

This manuscript has been authored by UT-Battelle, LLC under Contract No. DE-AC05-00OR22725 with the U.S. Department of Energy. The United States Government retains and the publisher, by accepting the article for publication, acknowledges that the United States Government retains a non-exclusive, paid-up, irrevocable, worldwide license to publish or reproduce the published form of this manuscript, or allow others to do so, for United States Government purposes. The Department of Energy will provide public access to these results of federally sponsored research in accordance with the DOE Public Access Plan (<http://energy.gov/downloads/doe-public-access-plan>).

## Observation of Real-Space Dynamic Electron Correlation in Beryllium

Rudra B. Bista<sup>1</sup>, \*Yuya Shinohara<sup>2</sup>, Wojciech Dmowski<sup>3</sup>, Chae Woo Ryu<sup>3,†</sup>, Jung Ho Kim<sup>4</sup>, Mary Upton<sup>4</sup>,  
Hlynur Gretarsson<sup>5</sup>, Martin Sundermann<sup>5</sup>, and \*Takeshi Egami<sup>1,2,3</sup>

<sup>1</sup>Department of Physics and Astronomy, The University of Tennessee, Knoxville, USA.

<sup>2</sup>Materials Science and Technology Division, Oak Ridge National Laboratory, USA.

<sup>3</sup>Department of Materials Science and Engineering, The University of Tennessee, Knoxville, USA.

<sup>4</sup>X-ray Science Division, Argonne National Laboratory, USA.

<sup>5</sup>Deutsches Elektronen-Synchrotron DESY, Germany.

<sup>†</sup>Current Address: Department of Materials Science and Engineering, Hongik University, Seoul 04066,  
South Korea.

\*Correspondence to: [egami@utk.edu](mailto:egami@utk.edu), [shinoharay@ornl.gov](mailto:shinoharay@ornl.gov)

### Abstract

Electron correlation in solid has a major impact on material properties. However, it has been studied mainly by theory, with very limited direct experimental investigations. Here, we report the results of real-space measurement of dynamic electron correlation using inelastic X-ray scattering on polycrystalline beryllium. The data are expressed as the energy-resolved dynamic pair-distribution function. Our results confirm the size of the exchange-correlation hole as  $\sim 2$  Å, consistent with theoretical expectations. However, at the plasmon energy of  $\sim 21$  eV, the exchange-correlation hole is extended up to 4-5 Å, suggesting a unique influence of the dynamic plasmon state.

The nearly-free electron theories in condensed matter physics are based on the idea that most fundamental physical phenomena in solids could be understood within a single-particle framework [1–3], even though electrons are dynamically correlated due to Coulomb interaction and constrained by the Pauli exclusion principle. This picture was supported by the Landau quasiparticle theory [4] and the density functional theory (DFT) [5]. Although the DFT has limitations in describing strongly correlated electron systems, which require many-body approaches such as the Hubbard model [3], it remains remarkably effective in explaining various phenomena in modern physics [6] and chemistry [7]. Electron correlation plays a central role in determining chemical bonding and material properties, and is likely a critical factor underlying emergent phenomena, such as superconductivity and charge ordering [8]. It also enables advanced applications including high-order harmonic generation [9], nanoscale single-electron sources [10], and single charge-based logic gates [11], making it a cornerstone of modern science and technology.

The DFT is based on the idea of exchange-correlation hole. Despite its significance, direct experimental observations of exchange-correlation hole remain scarce. Attempts have been made to observe exchange-correlation hole through the electronic pair-distribution function (PDF), which is obtained by Fourier-transforming the total electronic structure function,  $S(Q)$ , where  $Q$  is the momentum transfer in scattering, measured by X-ray diffraction [15–19]. In diffraction experiment a detector placed at a scattering angle,  $2\theta$ , measures,

$$S_{\text{Diff}}(Q_{\text{el}}) = \int S(Q(E), E) dE \quad (1)$$

where  $S(Q, E)$  is the dynamic structure factor accessible by inelastic scattering,  $E$  is the energy exchange in scattering, and  $Q_{\text{el}} = Q(E = 0)$ . Because  $Q$  varies with  $E$ ,  $S_{\text{Diff}}(Q_{\text{el}})$  is slightly different from  $S(Q)$ , for which the integration in Eq. (1) is made at a constant  $Q$ , making the PDF determined by diffraction measurement problematic, as discussed in Supplementary Information (SI). Furthermore, no attempt has been made to obtain information on dynamic electron correlation directly from the measurement of  $S(Q, E)$ .

In this article, we report on the observation of real-space dynamic electron correlation, using the real-space correlation function—specifically, the energy-resolved dynamic PDF,  $g(r, E)$ —which describes

spatial electron correlation as a function of excitation energy [20]. This method has previously been employed to observe dynamic atomic correlations [21], *e.g.*, the atomistic origins of relaxor ferroelectricity [22] and atom–atom correlations in superfluid  $^4\text{He}$  [23]. The  $g(r, E)$  is obtained by Fourier transforming the  $S(Q, E)$  over  $Q$ , by

$$g(r, E) = \frac{1}{2\pi^2\rho} \int S(Q, E) \frac{\sin Qr}{Qr} Q^2 dQ \quad (2)$$

with  $S(Q, E)$  measured over a wide  $Q$ -range to ensure accurate Fourier-transformation.

This conversion into the energy-resolved dynamic PDF facilitates the extraction of information on real-space dynamic correlations, whereas in the reciprocal space counterpart,  $S(Q, E)$ , such information is buried under the signals for electron excitations.  $S(Q, E)$  of electrons in light metals such as lithium, aluminum, and beryllium has been measured by using inelastic X-ray scattering (IXS) [17,19,24–28]. For a system of non-relativistic electron gas interacting with an electromagnetic field (X-rays), the Fermi’s golden rule shows that the non-resonant differential scattering cross section is, within the Born approximation, proportional to  $S(Q, E)$ , given by

$$S(Q, E = \hbar\omega) = \sum_{gf} \sum_{jj'} p_g \langle g | e^{-iQ \cdot r_j} | f \rangle \langle f | e^{iQ \cdot r_{j'}} | g \rangle \delta(E_g - E_f + \hbar\omega) \quad (3)$$

where  $|g\rangle$  and  $|f\rangle$  are the initial and the final states of the electron system,  $p_g$  is the probability of state  $|g\rangle$ , and  $E_g$  and  $E_f$  are the energies of states  $|g\rangle$  and  $|f\rangle$ , respectively [29,30]. The summation in terms of  $j$  and  $j'$  is over all electrons. By describing the response of the electron systems to an external electromagnetic field within a framework of linear response theory, the above equation is related to the response function of the system [31]:

$$S(Q, \omega) = \frac{1}{\pi} \frac{1}{1 - e^{-\beta\hbar\omega}} \chi''_{\rho^\dagger(Q)\rho(Q)}(\omega). \quad (4)$$

Here,  $\chi''_{\rho^\dagger(Q)\rho(Q)}(\omega)$  is the imaginary part of the electron density response function, and  $\rho(Q, t)$  is the electron density fluctuation operator, which is the spatial Fourier transform of the electron density operator defined by  $\rho(\mathbf{r}, t) = \sum_i \delta(\mathbf{r} - \mathbf{r}_i(t))$ . Most of the previous IXS studies of electrons in solids use this

description for the purpose of measuring single-particle excitations and collective excitations such as plasmons as shown in SI. However,  $S(\mathbf{Q}, \omega)$  can also be described in terms of the correlations in the density fluctuations in the system [32]. By using the Heisenberg time-dependent operator and by introducing the time-dependent correlation function of operators by  $\sum_i p_i \langle i | A(0)B(t) | i \rangle \equiv \langle A(0)B(t) \rangle$ , the dynamic structure factor is given by

$$S(\mathbf{Q}, \omega) = \frac{1}{2\pi\hbar} \int_{-\infty}^{\infty} dt e^{-i\omega t} \langle \rho(\mathbf{Q}, 0) \rho^\dagger(\mathbf{Q}, t) \rangle = \frac{1}{2\pi\hbar} \int G(\mathbf{r}, t) e^{i[\mathbf{Q} \cdot \mathbf{r} - \omega t]} d\mathbf{r} dt, \quad (5)$$

where  $G(\mathbf{r}, t)$  is the Van Hove correlation function [32],

$$G(\mathbf{r}, t) = \int \langle \rho(\mathbf{r} + \mathbf{r}', t) \rho(\mathbf{r}', 0) \rangle d\mathbf{r}'. \quad (6)$$

This representation provides a picture that the double-Fourier transformation of  $S(Q, E)$  describes the density-density correlation of electrons. Finally, the energy-resolved dynamic PDF,  $g(\mathbf{r}, E)$ , is obtained by performing the Fourier transformation of  $G(\mathbf{r}, t)$  over  $t$ :

$$g(\mathbf{r}, E) = \frac{1}{2\pi} \int G(\mathbf{r}, t) e^{-i(\frac{E}{\hbar})t} dt \quad (7)$$

Compared to the existing IXS works based on Eq. (4) that is suitable for describing the *response* of the system [33], this representation in real-space provides a more direct measure of the electron *correlation*. The information on electron correlation is included even in Eq. (4), but it is dispersed in  $Q$  space and is hardly visible. It becomes recognizable only when it is brought to real space. The Van Hove correlation function is useful when excitations decay with time [34], but when excitations are long-living, the energy-resolved dynamic PDF is more informative.

To obtain the energy-resolved dynamic PDF for electrons, we use beryllium as a testbed because it is a simple metal with few core-electrons, a high electronic density [35] and a weak ionic potential that keeps electrons nearly free [36]. As this work aims to directly observe the dynamic correlation of electrons in beryllium in real-space, we measure  $S(Q, E)$  of a polycrystalline beryllium plate at ambient conditions using medium-energy-resolution non-resonant IXS. The real-space dynamics are then extracted through the Fourier transformation of  $S(Q, E)$  over  $Q$ . While IXS measurements with conventional X-ray sources [37–

39] and synchrotron sources [18,24–28] have been reported for  $S(Q, E)$  in various solids for a range of purposes, including studies of the linear response function, plasmon dispersion and its linewidth [19,24,25,38–40], and the effect of band structure [26] within a lower  $Q$ -range (well below 5  $\text{\AA}^{-1}$ ), the real-space dynamic correlations of electrons have yet to be directly investigated.

One of the experimental challenges in the IXS of beryllium is its low X-ray absorption [41]. In transmission geometry, the low absorption results in an undesirably high background scattering originating from both the upstream and downstream of the sample. In reflection geometry, it leads to an exceptionally long footprint on the sample, complicating the normalization of the data. To mitigate systematic errors and artifacts specific to each experimental geometry, we carried out the IXS measurement in both transmission geometry and reflection geometry. The IXS measurement in transmission geometry was carried out using the spectrometer at 27ID-B in Advanced Photon Source (APS) at Argonne National Laboratory, and in reflection geometry using the spectrometer at P01 [42] in PETRA-III at DESY (See SI for details of experimental setting and data corrections). The incident X-ray energy was 11.32 keV and 9.7 keV in the transmission and reflection geometry, respectively. A polycrystalline beryllium plate of thickness 1.0 mm was used as the sample. Scattering data were recorded within a horizontal scattering geometry for the transmission measurements and a vertical scattering geometry for the reflection measurement. The scattering angles ( $2\theta$ ) spanned ranges of  $8^\circ < 2\theta < 90^\circ$  (transmission) and  $5^\circ < 2\theta < 160^\circ$  (reflection). At the APS, to maximize the scattering intensity at high angles in the horizontal setup, vertically polarized X-rays were produced by inserting a 250- $\mu\text{m}$ -thick diamond 220 phase retarder [43]. The spectra were measured over  $-4 < E/\text{eV} < 120$  with an overall resolution of 0.7 eV at the APS and over  $-10 < E/\text{eV} < 1000$  with an overall resolution of 1.4 eV at PETRA-III. The measured spectra,  $I(2\theta, E)$ , were corrected for sample absorption and X-ray polarization after the subtraction of elastic scattering, and were converted to  $S(Q, E)$ . The corrected spectra were then normalized using the  $f$ -sum rule to obtain the  $S(Q, E)$  for a single valence electron [19].

*Results* — Usually, IXS measurements are conducted to determine the dispersion of excitations, focusing on the peak positions and their width. For this study, however, we sought to determine  $S(Q, E)$  on an

absolute scale over a wide range of  $Q$ , which demands a higher level of accuracy than usual. By comparing the data collected in both geometries, we confirmed that most of the observed spectral features are intrinsic to the material. In this study, we analyzed the energy spectra up to  $E = 110$  eV, at which the X-ray Raman scattering is observed, resulting in  $S(Q, E)$  for beryllium as shown in Fig. 1. A sharp plasmon peak is observed around  $E = 21$  eV with little dispersion. Above  $Q = 2 \text{ \AA}^{-1}$ , the spectrum is dominated by Compton-like single-particle excitations. As numerous experiments have confirmed, plasmon excitations persist well beyond the critical wave vector  $Q_c = 1.24 \text{ \AA}^{-1}$  [37]. At  $Q < Q_c$ , plasmons are damped mainly due to interband transitions [19]. Beyond  $Q_c$  [44], damping intensifies as  $Q$  increases, primarily due to Landau damping [45]. At much higher  $Q$  ( $Q > 2Q_F$ , where  $Q_F = 1.94 \text{ \AA}^{-1}$  is the Fermi wave vector for Be), plasmon becomes completely damped. In addition to the valence contribution, the  $K$ -edge structure, referred to as

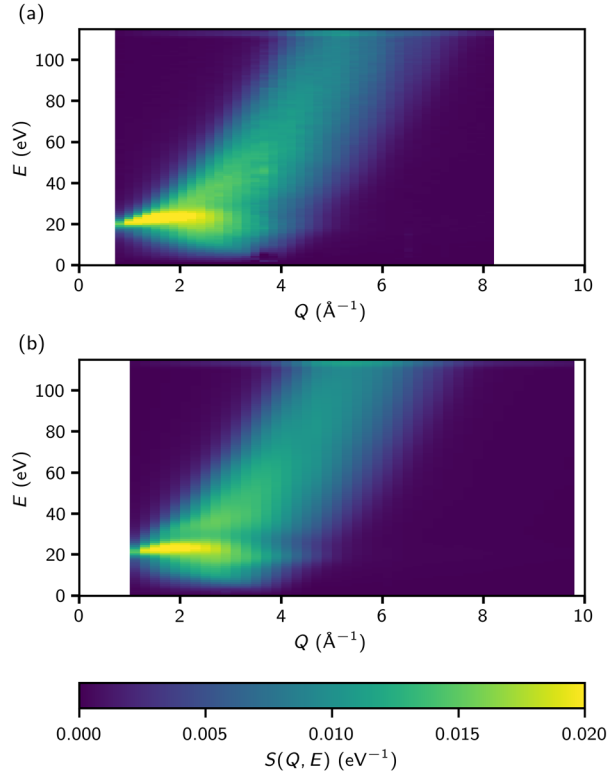


FIG. 1. Dynamic structure function,  $S(Q, E)$ , of electrons for beryllium measured at ambient condition. The  $S(Q, E)$  was obtained from IXS measurements in (a) a transmission geometry at 27ID-B in APS and (b) a reflection geometry at P01 in PETRA-III. Their color scales are shown at the bottom.

X-ray Raman scattering or Core-electron excitation, appears around 110 eV, with its intensity slightly increasing with  $Q$  [40,46].

The energy-resolved dynamic pair-distribution function,  $g(r, E)$ , which describes the spatial correlations of electrons at a specific excitation energy, can be obtained by the Fourier transformation of  $S(Q, E)$  over  $Q$  by Eq. (2). Fig. 2 presents a two-dimensional plot of  $g(r, E)$  for the electron system in polycrystalline beryllium.  $g(r, E) = 0$  corresponds to the average electron density. At  $r < 1 \text{ \AA}$ ,  $g(r, E)$  is dominated by information related to the self-motion of electrons. In this study, we focus on a higher  $r$ -range ( $r > 1 \text{ \AA}$ ) to examine the correlated dynamics of electrons. At  $E < 40 \text{ eV}$ , which is relevant to the DFT calculations, there is a strong depression in electron density below 2  $\text{\AA}$ . This depression signifies the exchange-correlation hole. Its size, approximately 2  $\text{\AA}$ , is consistent with the size of the exchange-correlation hole for electrons in beryllium as we discuss below.

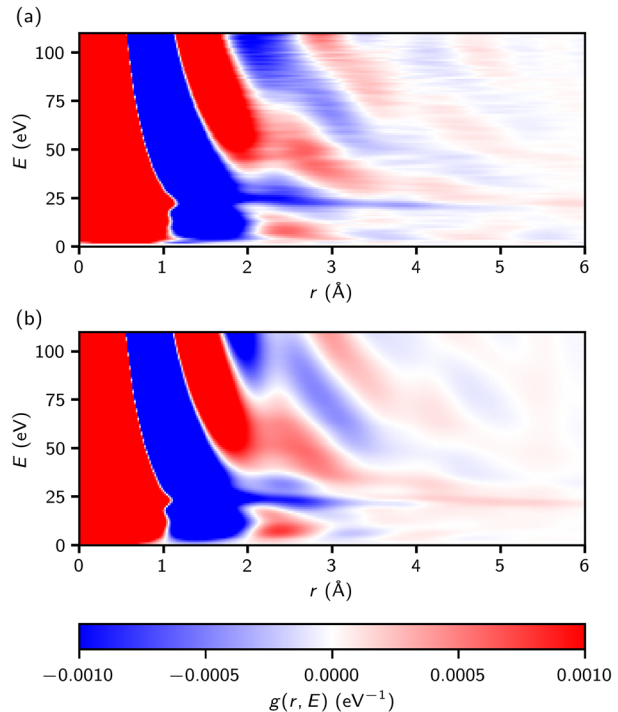


FIG. 2. Energy-resolved dynamic pair-distribution function,  $g(r, E)$ , of electrons in beryllium. The  $g(r, E)$  determined by the IXS in (a) the transmission geometry and (b) the reflection geometry is shown.

*Discussion* — This depression in  $g(r, E)$  shows a unique behavior near the plasmon energies around 21 eV. Fig. 3 shows  $g(r, E) \cdot E_F$  above, near and below the plasma frequency. To facilitate comparison with other systems, the dynamic PDF is made dimensionless by multiplying it by  $E_F$ . At 14 eV and 37 eV,  $g(r, E)$  oscillates around zero (average density) at distances beyond 2 Å, whereas at 21 eV, it is considerably depressed up to 4–5 Å. This result suggests that the exchange-correlation hole extends up to 4–5 Å in plasmon. Fig. 4 shows  $g(r, E)$  as a function of  $E$  at different distances, highlighting how the density depression extends in energy. As the distance increases, the depression associated with the exchange-correlation hole becomes progressively shallower and narrower, eventually disappearing at around 5 Å. These findings suggest that the collective electron dynamics within plasmon affects electron correlation, leading to an extended exchange-correlation hole. Slight differences between the APS data and the

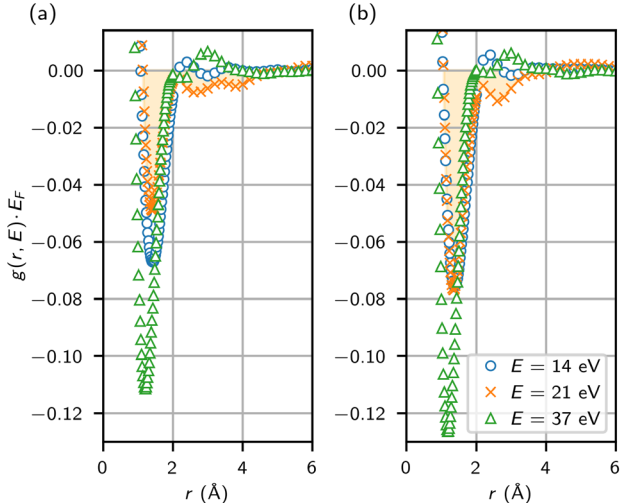


FIG. 3. Energy-sliced  $g(r, E)$  of electrons in beryllium determined in (a) the transmission geometry and (b) the reflection geometry. The size of the exchange correlation hole for plasmon is different from that of average electrons; the energy-slices at  $E = 14$  eV and 37 eV show the exchange-correlation hole for average electrons, which is roughly 2 Å, while at  $E = 21$  eV, corresponding to plasmons, reveals a larger spatial extent of approximately 5 Å in (a) the transmission geometry and 4.2 Å in (b) the reflection geometry.

PETRA-III data illustrate the extent of systematic errors arising from differences in experimental geometry and setup. However, these differences are insignificant and do not affect the overall conclusions.

There are intensity oscillations in  $g(r, E)$  along  $r$  as shown in Fig. 3, but these oscillations are intrinsic to the data and are not artifacts of termination errors. While all PDFs are inherently affected by termination effects due to the limited  $Q$ -range, these effects produce oscillations with a characteristic wavelength  $\lambda_t = 2\pi/Q_{\max}$ , where  $Q_{\max}$  is the upper limit of the  $Q$  range. In this study,  $\lambda_t = 0.6\text{-}0.7 \text{ \AA}$ , which is considerably shorter than the observed oscillation wavelength of  $\sim 1.4 \text{ \AA}$ , suggesting that these oscillations are not a consequence of termination errors. Instead, they are more likely attributable to the self-term, representing outgoing spherical waves of photoelectrons produced by Compton scattering. This subject will be discussed elsewhere.

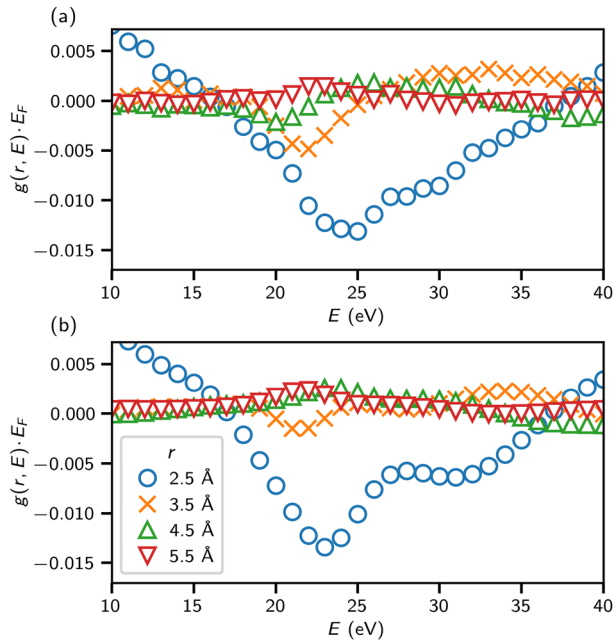


FIG. 4. Distance-sliced  $g(r, E)$  of electrons in beryllium: This illustrates the energy dependence of the density depression in  $g(r, E)$  at various fixed radial distances,  $r$ . As  $r$  increases from  $2.5 \text{ \AA}$ , the dip becomes progressively shallower and shifts to lower energy, eventually disappearing at  $5.5 \text{ \AA}$  in (a) the transmission geometry and  $4.5 \text{ \AA}$  in (b) the reflection geometry.

The single particle excitations are suppressed below the plasmon energy. Thus, the exchange-correlation hole relevant to DFT is most appropriately evaluated in the energy range below the plasmon energy. As shown in Fig. 3, the exchange-correlation hole is well-defined with a size of approximately 2 Å and exhibits a strong depression of pair-density for distances less than 2 Å. However, the exchange-correlation hole appears to decrease in size with increasing energy (Fig. 2). This observation is misleading because  $g(r, E)$  above the plasmon energy is dominated by the contribution from the self-term. The snapshot  $g(r)$  is calculated by integrating  $g(r, E)$  over  $E$ , and theoretically, the self-term at  $r \neq 0$  should cancel out completely upon energy integration. Nevertheless, the strength of the self-term evident in Fig. 2 highlights that any experimental error could disrupt this cancellation, raising concerns about the reliability of the snapshot PDF obtained by diffraction measurements.

The size of the exchange-correlation hole,  $r_{xc}$ , depends on the valence electron density,  $\rho_{ele}$ . For beryllium ( $\rho_{ele} = 0.247 \text{ \AA}^{-3}$ ),  $r_{xc}$  is estimated to be approximately 2 Å, which closely matches our observed value (see SI for details). Besides, Perdew and Wang [47] developed an analytical method to construct the coupling-constant average pair-distribution function,  $g(r, r')$ , for a uniform electron gas with various density parameters. Their method was validated using Quantum Monte Carlo simulations [48,49] for both spin-polarized and spin-unpolarized systems. For beryllium, their result predicts  $r_{xc} \sim 2 \text{ \AA}$  from the depletion in the exchange-correlation hole density given by  $\rho_{xc}(r, r') = \rho(r')[g(r, r') - 1]$ , which is consistent with the results presented here (details in SI).

The extended exchange-correlation hole at the plasma frequency is likely attributed to plasmon dynamics. Within the plasmon, electrons move cooperatively with a reduced probability of impinging on each other, leading to a larger exchange-correlation hole. This observation may provide insight into an earlier observation on  ${}^4\text{He}$ . Through the energy-resolved dynamic PDF, it was found that the He-He distance in the Bose-Einstein (BE) condensate is longer by 10 % compared to that in the non-condensate [23]. In the BE condensate, atoms are in the ground state without momentum, thus they do not impinge on each other just as in the plasmon, explaining the increased He-He distance. The cut-off momentum,  $Q_c = 1.24 \text{ \AA}^{-1}$ ,

characterizes the range of cooperative electron dynamics. Correspondingly, the associated wavelength, 5.1 Å, may define the spatial extent of the extended exchange-correlation hole at the plasma frequency.

*Conclusion*— Our study demonstrates that real space dynamic correlations among electrons can be directly observed by IXS using the energy-resolved dynamic PDF. The results highlight distinct differences in correlation dynamics above, near, and below the plasma frequency. In particular, within the energy range relevant to the DFT calculations, the exchange-correlation hole is sharply defined with a size of  $\sim$ 2 Å, consistent with theoretical estimations. This result contrasts with the conventional snapshot PDF approach obtained by diffraction without energy discrimination, which is prone to inaccuracies due to the possible errors at high energy transfers. Furthermore, the results highlight that the exchange-correlation hole associated with plasmons is more spatially extended, possibly due to cooperative electron dynamics intrinsic to the plasmon. This finding provides concrete evidence that electron correlation is affected by electron dynamics. The insights into real-space dynamic electron correlations, enabled by the energy-resolved dynamic PDF method, offers strong support for the DFT framework of electron correlation. These results also confirm that the measured dynamic structure function encodes information not only about single particle excitations but also about dynamic electron correlations. This study provides opportunities to explore and deepen our understanding of correlated electron dynamics, shedding critical new light on the broader field of condensed matter physics.

**Acknowledgements**— This work was supported by U.S. Department of Energy (DOE), Office of Science, Office of Basic Energy Sciences, Division of Materials Sciences and Engineering. This research used resources of the Advanced Photon Source, a U.S. DOE Office of Science User Facility operated for the DOE Office of Science by Argonne National Laboratory under Contract No. DE-AC02-06CH11357. We acknowledge DESY (Hamburg, Germany), a member of the Helmholtz Association HGF, for the provision of experimental facilities. Part of this research were carried out at PETRA III. Data was collected using

P01 operated by DESY Photon Science. Beamtime was allocated for proposal I-20230998. At the APS beamtime was allocated for proposal 80535.

## References

- [1] D. Bohm and D. Pines, A Collective Description of Electron Interactions: III. Coulomb Interactions in a Degenerate Electron Gas, *Phys. Rev.* **92**, 609 (1953).
- [2] M. Gell-Mann and K. A. Brueckner, Correlation Energy of an Electron Gas at High Density, *Phys. Rev.* **106**, 364 (1957).
- [3] J. Hubbard, The Description of Collective Motions in Terms of Many-Body Perturbation Theory. II. The Correlation Energy of a Free-Electron Gas, *Proc. R. Soc. Lond. A* **243**, 336 (1958).
- [4] L. Landau, Theory of Fermi Liquids, *Sov. Phys. JETP* **3**, 920 (1956).
- [5] W. Kohn and L. J. Sham, Self-Consistent Equations Including Exchange and Correlation Effects, *Phys. Rev.* **140**, A1133 (1965).
- [6] R. Dörner, V. Mergel, O. Jagutzki, L. Spielberger, J. Ullrich, R. Moshammer, and H. Schmidt-Böcking, Cold Target Recoil Ion Momentum Spectroscopy: a ‘momentum microscope’ to view atomic collision dynamics, *Physics Reports* **330**, 95 (2000).
- [7] H. J. Wörner et al., Conical Intersections Dynamics in NO<sub>2</sub> Probed by Homodyne High-Harmonic Spectroscopy, *Science* **334**, 208 (2011).
- [8] R. Haindl, A. Feist, T. Domröse, M. Möller, J. H. Gaida, S. V. Yalunin, and C. Ropers, Coulomb-correlated electron number states in a transmission electron microscope beam, *Nat. Phys.* **19**, 1410 (2023).
- [9] S. Sukiasyan, C. McDonald, C. Destefani, M. Yu. Ivanov, and T. Brabec, Multielectron Correlation in High-Harmonic Generation: A 2D Model Analysis, *Phys. Rev. Lett.* **102**, 223002 (2009).
- [10] G. Fève, A. Mahé, J.-M. Berroir, T. Kontos, B. Plaçais, D. C. Glattli, A. Cavanna, B. Etienne, and Y. Jin, An On-Demand Coherent Single-Electron Source, *Science* **316**, 1169 (2007).
- [11] M. A. Kastner, The single-electron transistor, *Rev. Mod. Phys.* **64**, 849 (1992).
- [12] E. Wigner and F. Seitz, On the Constitution of Metallic Sodium, *Phys. Rev.* **43**, 804 (1933).
- [13] J. C. Slater, The Electronic Structure of Metals, *Rev. Mod. Phys.* **6**, 209 (1934).
- [14] P. Fulde, *Electron Correlations in Molecules and Solids*, Third (Springer-Verlag Berlin Heidelberg GmbH, Berlin, 2002).
- [15] W. Schülke, U. Berg, and O. Brümmer, Evidence for the Coulomb Interaction of Be Valence Electrons by Compton Scattering Cross-Section Measurements, *Phys. Stat. Sol. (b)* **35**, 227 (1969).
- [16] G. Mazzone, F. Sacchetti, and V. Contini, Static structure factor and electron-electron correlations in Be. A comparison of experiment with electron-gas theory, *Phys. Rev. B* **28**, 1772 (1983).
- [17] V. Contini and F. Sacchetti, Electron-electron correlation in beryllium and related properties, *J. Phys. F: Met. Phys.* **11**, L1 (1981).

- [18] P. Eisenberger, W. C. Marra, and G. S. Brown, Measurement of the Static Structure Factor for Conduction Electrons with Use of Synchrotron Radiation, *Phys. Rev. Lett.* **45**, 1439 (1980).
- [19] W. Schülke, *Electron Dynamics by Inelastic X-Ray Scattering* (Oxford University Press, Oxford, 2007).
- [20] T. Egami and W. Dmowski, Dynamic pair-density function method for neutron and X-ray inelastic scattering, *Zeitschrift Für Kristallographie* **227**, 233 (2012).
- [21] K. A. Acosta, H. C. Walker, and A. M. Fry-Petit, Optimizing the dynamic pair distribution function method for inelastic neutron spectrometry, *Nat. Rev. Phys.* **5**, 236 (2023).
- [22] W. Dmowski, S. B. Vakhrushev, I.-K. Jeong, M. P. Hehlen, F. Trouw, and T. Egami, Local Lattice Dynamics and the Origin of the Relaxor Ferroelectric Behavior, *Phys. Rev. Lett.* **100**, 137602 (2008).
- [23] W. Dmowski, S. O. Diallo, K. Lokshin, G. Ehlers, G. Ferré, J. Boronat, and T. Egami, Observation of dynamic atom-atom correlation in liquid helium in real space, *Nat Commun* **8**, 15294 (2017).
- [24] W. Schülke, H. Nagasawa, S. Mourikis, and P. Lanzki, Dynamic structure of electrons in Li metal: Inelastic synchrotron x-ray scattering results and interpretation beyond the random-phase approximation, *Phys. Rev. B* **33**, 6744 (1986).
- [25] W. Schülke, H. Schulte-Schrepping, and J. R. Schmitz, Dynamic structure of electrons in Al metal studied by inelastic x-ray scattering, *Phys. Rev. B* **47**, 12426 (1993).
- [26] W. Schülke, H. Nagasawa, S. Mourikis, and A. Kaprolat, Dynamic structure of electrons in Be metal by inelastic x-ray scattering spectroscopy, *Phys. Rev. B* **40**, 12215 (1989).
- [27] P. M. Platzman, E. D. Isaacs, H. Williams, P. Zschack, and G. E. Ice, X-ray-scattering determination of the dynamic structure factor of Al metal, *Phys. Rev. B* **46**, 12943 (1992).
- [28] B. C. Larson, J. Z. Tischler, E. D. Isaacs, P. Zschack, A. Fleszar, and A. G. Eguiluz, Inelastic X-Ray Scattering as a Probe of the Many-Body Local-Field Factor in Metals, *Phys. Rev. Lett.* **77**, 1346 (1996).
- [29] W. Schülke, *Inelastic Scattering by Electronic Excitations*, in *Handbook on Synchrotron Radiation*, Vol. 3 (Elsevier, 1991), pp. 565–637.
- [30] S. K. Sinha, Theory of inelastic x-ray scattering from condensed matter, *J. Phys.: Condens. Matter* **13**, 7511 (2001).
- [31] D. Pines and P. Nozières, *The Theory of Quantum Liquids* (W. A. Benjamin Inc., 1966).
- [32] L. Van Hove, Correlations in Space and Time and Born Approximation Scattering in Systems of Interacting Particles, *Phys. Rev.* **95**, 249 (1954).
- [33] P. Abbamonte, K. D. Finkelstein, M. D. Collins, and S. M. Gruner, Imaging Density Disturbances in Water with a 41.3-Attosecond Time Resolution, *Phys. Rev. Lett.* **92**, 237401 (2004).
- [34] T. Egami and Y. Shinohara, Perspective: Correlated atomic dynamics in liquid seen in real space and time, *J. Chem. Phys.* **153**, 180902 (2020).
- [35] N. W. Ashcroft and N. D. Mermin, *Solid State Physics* (Saunders College Publishing, 1976).
- [36] M. Y. Chou, P. K. Lam, and M. L. Cohen, *Ab initio* study of structural and electronic properties of beryllium, *Phys. Rev. B* **28**, 4179 (1983).
- [37] P. Eisenberger, P. M. Platzman, and K. C. Pandy, Investigation of X-Ray Plasmon Scattering in Single-Crystal Beryllium, *Phys. Rev. Lett.* **31**, 311 (1973).

- [38] A. Vradis and G. D. Priftis, Dynamic structure factor  $S(k,\omega)$  of beryllium by x-ray inelastic scattering experiments, *Phys. Rev. B* **32**, 3556 (1985).
- [39] P. M. Platzman and P. Eisenberger, Presence of an Incipient Wigner Electron Lattice in Solid-State Electron Gases, *Phys. Rev. Lett.* **33**, 152 (1974).
- [40] T. Suzuki and A. Tanokura, X-ray Plasmon Scattering. I. Experiment on Beryllium, *J. Phys. Soc. Jpn.* **29**, 972 (1970).
- [41] D. C. Creagh and J. H. Hubbel, *X-Ray Absorption (or Attenuation) Coefficients*, in *International Tables for Crystallography*, Vol. C (International Union of Crystallography, 2006), pp. 220–229.
- [42] D. Ketenoglu et al., X-ray Raman spectroscopy of lithium-ion battery electrolyte solutions in a flow cell, *J Synchrotron Rad* **25**, 537 (2018).
- [43] K. Hirano, T. Ishikawa, and S. Kikuta, Development and application of x-ray phase retarders (invited), *Review of Scientific Instruments* **66**, 1604 (1995).
- [44] M. Hasegawa and M. Watabe, Theory of Plasmon Damping in Metals. I. General Formulation and Application to an Electron Gas, *J. Phys. Soc. Jpn.* **27**, 1393 (1969).
- [45] L. Landau, On the vibrations of the electronic plasma, *J. Phys. U.S.S.R.* **10**, 25 (1946).
- [46] H. Nagasawa, S. Mourikis, and W. Schülke, X-Ray Raman Spectrum of Li, Be and Graphite in a High-Resolution Inelastic Synchrotron X-Ray Scattering Experiment, *J. Phys. Soc. Jpn.* **58**, 710 (1989).
- [47] J. P. Perdew and Y. Wang, Pair-distribution function and its coupling-constant average for the spin-polarized electron gas, *Phys. Rev. B* **46**, 12947 (1992).
- [48] D. Ceperley, Ground state of the fermion one-component plasma: A Monte Carlo study in two and three dimensions, *Phys. Rev. B* **18**, 3126 (1978).
- [49] D. M. Ceperley and B. J. Alder, Ground State of the Electron Gas by a Stochastic Method, *Phys. Rev. Lett.* **45**, 566 (1980).

## Supplementary Information for “Observation of Real-Space Dynamic Electron Correlation in Beryllium”

Rudra B. Bista<sup>1</sup>, \*Yuya Shinohara<sup>2</sup>, Wojciech Dmowski<sup>3</sup>, Chae Woo Ryu<sup>3,†</sup>, Jung Ho Kim<sup>4</sup>, Mary Upton<sup>4</sup>, Hlynur Gretarsson<sup>5</sup>, Martin Sundermann<sup>5</sup>, and \*Takeshi Egami<sup>1,2,3</sup>

<sup>1</sup>Department of Physics and Astronomy, The University of Tennessee, Knoxville, USA.

<sup>2</sup>Materials Science and Technology Division, Oak Ridge National Laboratory, USA.

<sup>3</sup>Department of Materials Science and Engineering, The University of Tennessee, Knoxville, USA.

<sup>4</sup>X-ray Science Division, Argonne National Laboratory, USA.

<sup>5</sup>Deutsches Elektronen-Synchrotron DESY, Germany.

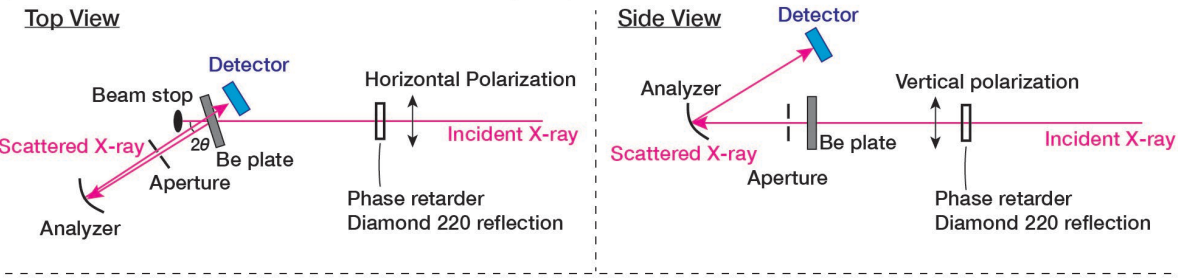
<sup>†</sup>Current Address: Department of Materials Science and Engineering, Hongik University, Seoul 04066, South Korea.

\*Correspondence to: [egami@utk.edu](mailto:egami@utk.edu), [shinoharay@ornl.gov](mailto:shinoharay@ornl.gov)

### Supplementary Note 1. Experimental configurations

Figure S1 shows schematics of the experimental configurations at two beamlines: (top) 27ID-B at the Advanced Photon Source (APS) and (bottom) P01 at PETRA III. Measurements at 27ID-B, APS, were conducted in transmission geometry with 11.32 keV X-rays. Scattering data were recorded within a horizontal scattering geometry. The beam size at the sample position perpendicular to the X-ray propagation was 50  $\mu\text{m}$  (H)  $\times$  4  $\mu\text{m}$  (V). The incident angle of X-ray on the sample was 45°, and the scattered X-rays

#### Schematic view of IXS measurement at 27ID-B, APS



#### Side view of IXS measurement at P01, PETRA-III

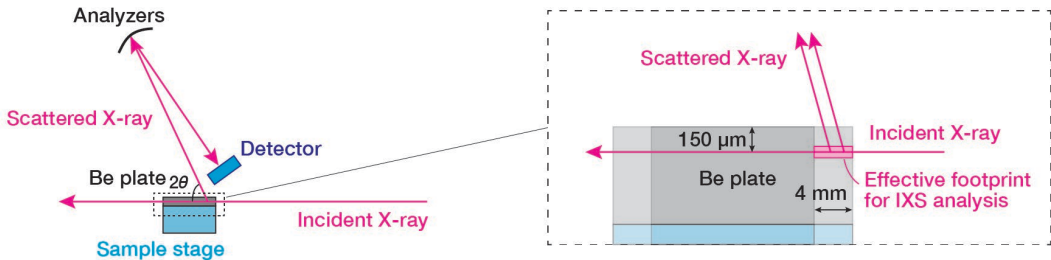


FIG. S1. Experimental configurations: These schematics highlight the differences in configuration at (top) 27ID-B, APS and (bottom) P01 at PETRA III. Only the main components are shown and not all the optics including monochromator is included in this figure.

were analyzed by a Si (844) diced spherical backscattering analyzer with a curvature of 1 m and collected using a CdTe LAMBDA 60k 2D detector, providing an overall energy resolution of 0.7 eV. The spectra were measured over the interval  $-4 < E/\text{eV} < 120$ . An aperture installed between the sample and the analyzer defined the momentum resolution of  $0.2 \text{ \AA}^{-1}$ . The incident X-ray beam polarized to approximately 80% vertical polarization which was achieved by using a 250- $\mu\text{m}$ -thick diamond 220 phase retarder.

Measurements at P01, PETRA-III, were performed in reflection geometry with 9.7 keV X-rays. Scattering data were recorded within a vertical scattering geometry. Scattered X-rays were analyzed by four Si (660) spherically bent backscattering analyzers, and the overall energy resolution was 1.4 eV. A Silicon 2D Medipix3 based Lambda detector was used to record the scattering data. The spectra were measured over  $-10 < E/\text{eV} < 1000$ . X-rays were incident from the side of the sample to minimize background scattering from the sample stage as shown in Fig. S1. The horizontally polarized X-rays of a beam size  $200 \mu\text{m} (\text{H}) \times 20 \mu\text{m} (\text{V})$  was incident at  $150 \mu\text{m}$  below the sample surface. Due to the beam's footprint being relatively long, as indicated by the shaded area in the schematic, angular resolution was optimized by restricting the effective footprint on the sample to 4 mm along the beam direction. To achieve this, a set of elastic scattering measurements were conducted at each  $2\theta$  by shifting the sample position along the direction of the incident X-ray beam, and the region of interest (ROI) on the LAMBDA detector was defined by taking the difference of the two elastic scattering data.

### Supplementary Note 2. Normalization of the inelastic X-ray scattering spectra

If inelastic X-ray scattering spectra over infinite  $E$ -range is accessible, the  $f$ -sum rule could be applied at each  $Q$  to correct and normalize the spectra [S1]. However, the actual measurements are limited to a finite  $E$ -range, which restricts the ability to normalize the spectra over entire  $Q$ -range solely using the  $f$ -sum rule, in particular at high  $Q$  where parts of the single-electron excitation signal lie outside the accessible  $E$ -range. Therefore, we first consider  $Q$ -dependent corrections related to sample absorption and X-ray polarization [S2], and the  $f$ -sum rule was used afterwards to convert the spectra into the absolute scale. The measured spectra,  $I(2\theta, E)$ , were corrected for sample absorption and X-ray polarization after the subtracting elastic scattering and converting coordinate from  $2\theta$ -space to  $Q$ -space, and were subsequently converted to dynamic structure factor,  $S(Q, E)$ . Here, elastic scattering was modeled using a Voigt function and subtracted from the spectra.

At PETRA-III, the measurement was conducted in the vertical scattering plane as discussed in the previous section, making the polarization correction negligible and therefore it was omitted. At APS, the measurement was performed in the horizontal plane, where the polarization factor for a perfectly horizontally polarized X-ray is expressed as  $\cos^2 2\theta$ . In this geometry, little scattering intensity is expected near  $2\theta = 90^\circ$ . To overcome this issue, a diamond phase retarder was introduced to enhance the proportion of vertically polarized X-rays in the beam, which was estimated to be 70-90 %. Given the uncertainty in the degree of vertical polarization, we calculated the dynamic PDF using several assumed values of vertical polarization: 70, 80, and 90 % as shown in Fig. S2. The differences in results due to the uncertainty in vertical polarization are minor. For the main text, we used results corresponding to 80 % vertical polarization, which also showed good agreement with measurement conducted at PETRA-III as shown in the main text.

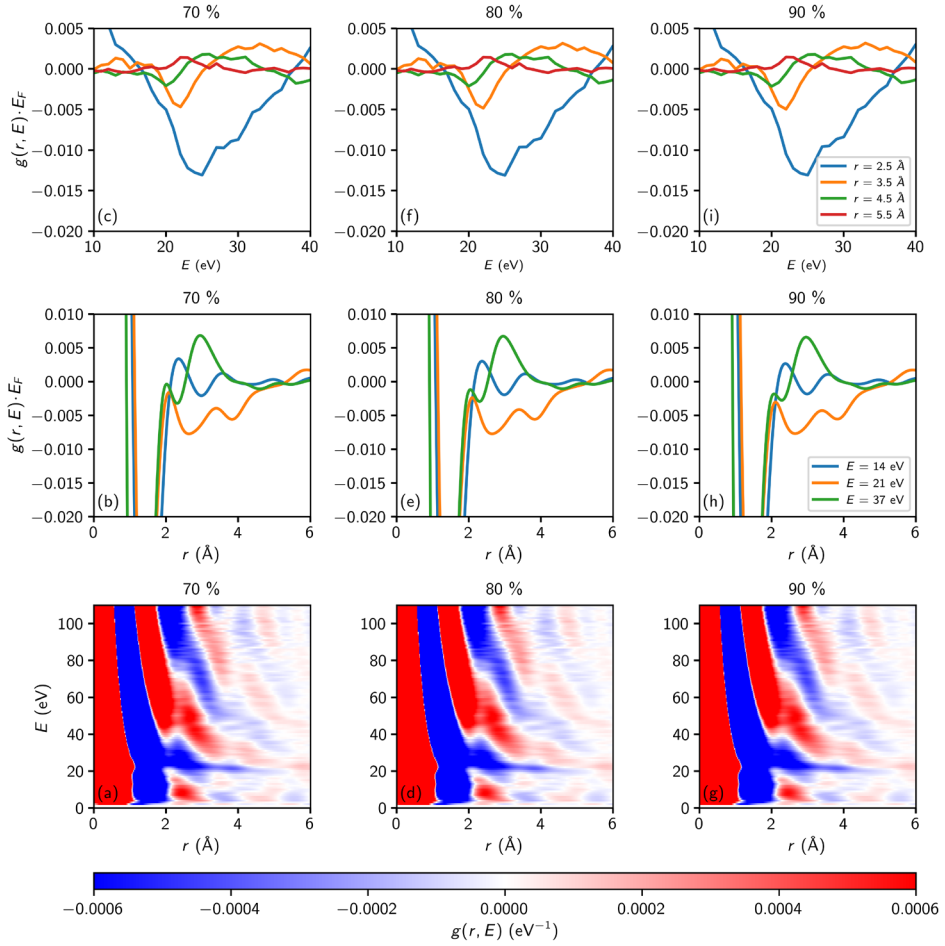


FIG. S2. Effect of the degree of polarization on the energy-resolved dynamic PDF of electrons in beryllium: The  $g(r, E)$  was calculated by using the IXS taken at APS (Bottom) Image plots, (middle) the energy-slices at 14, 21, and 37 eV, and (top) the constant- $r$  slices at 2.5, 3.5, 4.5 and 5.5 Å, illustrating the effect of vertical polarization values: (a, b, c) 70%, (d, e, f) 80%, and (g, h, i) 90%.

After correcting the scattering intensity in terms of absorption and polarization, the spectra was brought to an absolute scale by applying the  $f$ -sum rule [S3]:

$$\int_0^\infty dES(Q, E)E = \frac{n\hbar^2 Q^2}{2m} \quad (S1)$$

where  $n$  and  $m$  denote the number of electrons per atom for Be and the electron mass, respectively. For the data taken at APS, the highest energy transfer used for the integration was 110 eV, below which the core excitation can be ignored. This constraint limits the normalization using the  $f$ -sum rule up to  $Q = 3.8 \text{ \AA}^{-1}$ , beyond which the major portion of the valence electron signal starts to overlap with the core excitation signal as shown in Fig. S3, where  $S_m(Q, E)$  is all corrected measured spectra. Therefore, we used a single normalization constant that was estimated by the values in  $1.7 < Q/\text{\AA}^{-1} < 3.0$  to normalize the entire spectra for the data taken at APS. For the data taken at PETRA-III, the data up to 1000 eV were used, and the  $f$ -

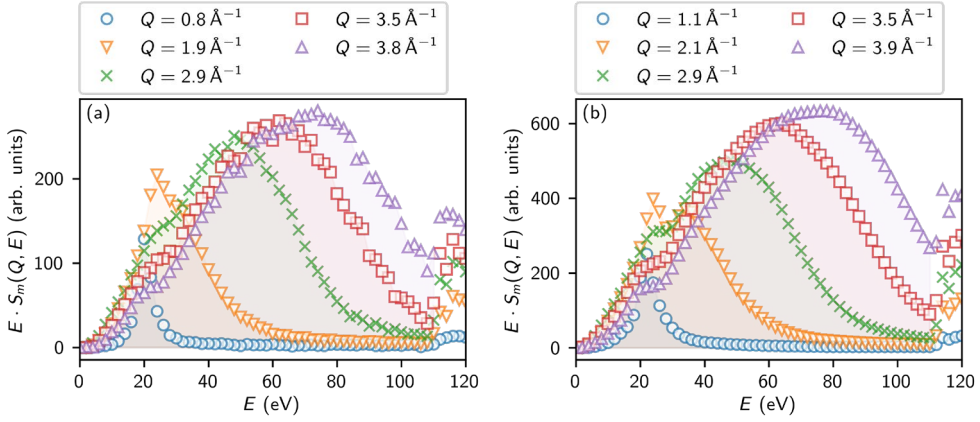


FIG. S3. Energy-weighted spectra  $E \cdot S_m(Q, E)$  for beryllium at selected  $Q$  values: The shaded area ( $E < 110$  eV,  $Q < 3.8 \text{ \AA}^{-1}$ ) represents the range used to determine the normalization constant for both (a) APS data and (b) PETRA-III data.

sum rule for both the valence electrons (using the spectra up to 110 eV) and total electrons were used for assessing the self-consistency.

The  $f$ -sum integral at each  $Q$  is compared with the theoretical values as shown in Fig. S4. The  $f$ -sum rule integral follows a  $Q^2$  power law at lower  $Q$  values up to approximately  $3.8 \text{ \AA}^{-1}$ , but the discrepancy is found at higher  $Q$  values, which is due to a limited energy range for the sum integral.

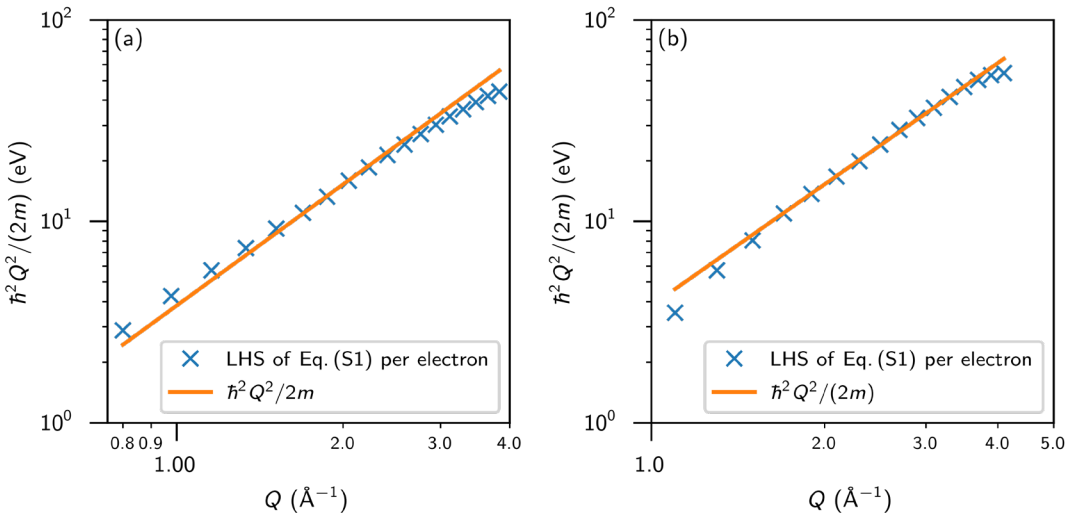


FIG. S4.  $f$ -sum rule integration and normalization constant: The  $f$ -sum rule integration of a measured data (crosses, the LHS of Eq. (S1) per one electron) is compared with the theoretical  $f$ -sum values,  $\hbar^2 Q^2/(2m)$ , (a) for a valence electron taken at the APS and (b) a total electron taken at PETRA-III.

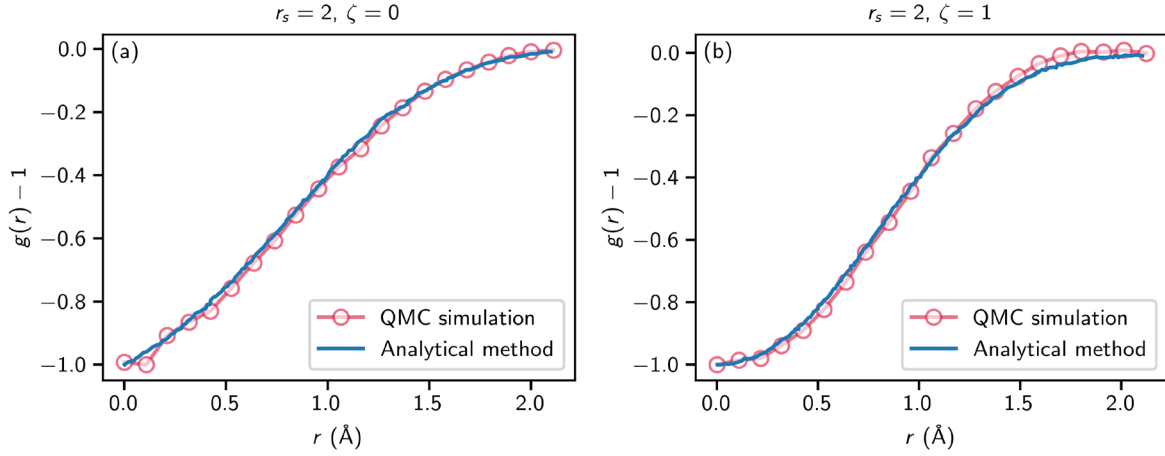


FIG. S5. Estimate of the size of the exchange-correlation hole of electrons in beryllium ( $r_s \sim 2$ ) using pair-distribution function. The value of  $r_{xc}$  is estimated to be  $\sim 2$  Å in both the analytical method by Perdue and Wang [S5] and QMC simulations [S6,S7], represented by a blue dense line and red circles, respectively. (a) Spin-unpolarized electrons ( $\zeta = 0$ ) and (b) fully spin-polarized electrons ( $\zeta = 1$ ).

**Supplementary Note 3. Estimating the size of the exchange-correlation hole of valence electrons in beryllium using electron density.**

The electron density,  $\rho$ , is related to the effective electron spacing,  $r_0$ , by

$$\rho = \frac{3}{4\pi r_0^3}. \quad (S2)$$

For beryllium, the valence electron density is  $0.247 \text{ \AA}^{-3}$ , leading to  $r_0 = 0.99 \text{ \AA}$  [S4]. Since the distance between two electrons provides an estimate of the size of exchange-correlation hole, its size is estimated to be  $r_{xc} = 2r_0 = 1.98 \text{ \AA}$ . This agrees with our observed results for average electrons in beryllium as discussed in the main text.

**Supplementary Note 4. Estimating the size of the exchange-correlation hole of valence electrons in beryllium using pair-distribution function.**

We approximate the size of exchange-correlation hole  $r_{xc}$ , using the pair-distribution function  $g(r, r')$  of a homogeneous electron gas, defined by the probability of finding an electron at point  $r'$  provided there is another electron at  $r$ . Perdue and Wang et al. [S5] developed an analytical method to construct the coupling-constant average pair-distribution function  $g(r, r')$  for a uniform electron gas with density parameters ( $r_s = 2, 5, 10$ ) and compared it with Quantum Monte Carlo simulations [S6,S7] for both spin-polarized and spin-unpolarized systems. For beryllium ( $r_s \sim 2$ ), the value of  $r_{xc}$  is determined to be approximately 2 Å, as shown in Fig. S5 (a) for a spin-unpolarized electrons ( $\zeta = 0$ ) and (b) fully spin-polarized electrons ( $\zeta = 1$ ). This determination is based on the depletion in density due to the exchange-correlation hole around an electron at position  $r$ , given by  $\rho_{xc}(r, r') = \rho(r')[g(r, r') - 1]$ , assuming  $\rho(r')$  is uniform, which is consistent with our observed results.

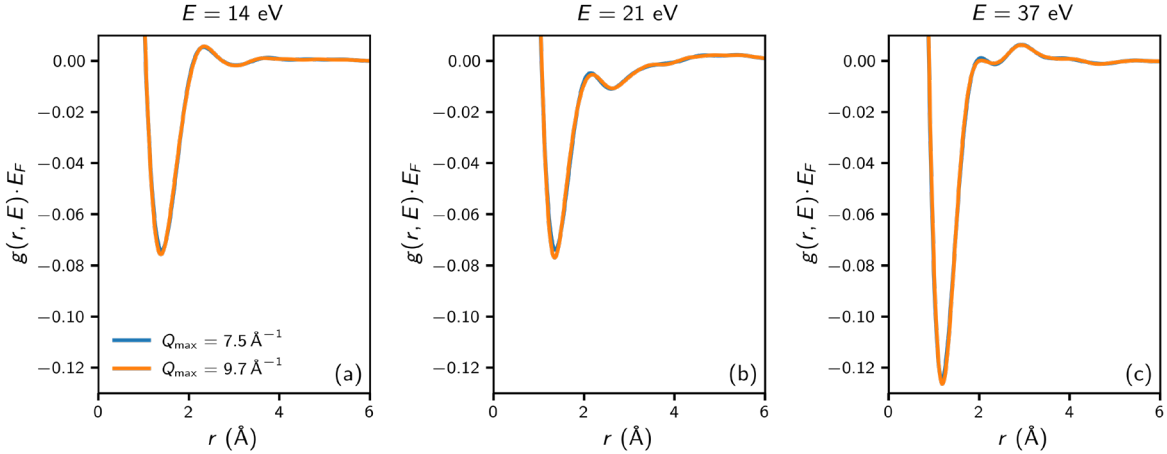


FIG. S6. Effect of finite  $Q$ -range on the Fourier transform over  $Q$ . By using different cutoffs ( $Q_{\max} = 9.7 \text{ \AA}^{-1}$  and  $7.5 \text{ \AA}^{-1}$ ), the profiles of  $g(r, E)$  at 14, 21, and 37 eV were calculated, showing a minor influence of the finite  $Q$ -range on the results.

#### Supplementary Note 5. Effect of finite $Q$ -range on the calculation of $g(r, E)$

When calculating the Fourier transform, the effect of finite data range needs to be carefully examined. To examine the effect of the finite  $Q$ -range on the calculation of  $g(r, E)$ , we calculated the Fourier transformation of selected IXS spectrum taken at the PETRA III data from  $Q$ -space to real-space  $r$  at two cutoffs,  $Q_{\max} = 9.7 \text{ \AA}^{-1}$  and  $Q_{\max} = 7.5 \text{ \AA}^{-1}$ , for three representative energies: 14 eV, 21 eV and 37 eV, as shown in Fig. S6. This clearly demonstrates that the impact of the termination errors on our results in  $g(r, E)$  is negligible, as discussed in the main text.

#### Supplementary Note 6. The cumulative integral of energy-resolved dynamic PDF over energy transfer

As discussed in the main text, the high-energy region of  $S(Q, E)$  is dominated by the self-part, or the single-particle excitation spectrum, which theoretically goes to zero after the energy integration to obtain  $S(Q)$ . Therefore, the contribution from the self-part to  $g(r, E)$  should integrate out to zero. In reality, however, because of the limited range of  $E$  the cancellation is incomplete. To illustrate this behavior, we compute the energy integrated dynamic PDF or the cumulative integral of energy-resolved dynamic PDF,  $I_{\text{cum}}(E)$ , over energy transfer defined as [S8]

$$I_{\text{cum}}(E) = \frac{1}{r_2 - r_1} \int_0^E \int_{r_1}^{r_2} \Delta g(r, E') \, dr \, dE'. \quad (\text{S3})$$

The function  $I_{\text{cum}}(E)$  quantifies the contribution of both negative and positive correlations in the dynamic PDF at the range from  $r_1$  to  $r_2$  to the total snapshot PDF,  $g(r)$ . As an example, we chose  $r_1 = 1.5 \text{ \AA}$  and  $r_2 = 1.7 \text{ \AA}$ . This specific range of  $r$  was chosen because for  $r < 1 \text{ \AA}$ , the self-term dominates entirely, while at larger  $r$ , electron correlation becomes negligible. Thus, the selected range of  $r_1$  and  $r_2$  represent an optimal range for capturing the effect of energy-integral range on the snapshot PDF at the  $r$ -range where the

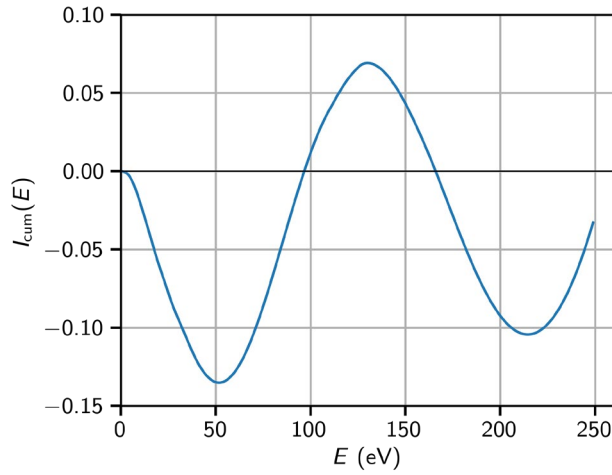


FIG. S7. The integrated dynamic PDF as a function of energy transfer: There is a significant variation of the cumulative integral of dynamic PDF represented by equation (S3) with energy transfer  $E$ , whereas it should converge at higher energy transfers.

exchange-correlation hole is significant. The pronounced variation of  $I_{\text{cum}}(E)$  with respect to  $E$  is shown in Fig. S7. At  $r = 1.6 \text{ \AA}$  the integration should converge around  $g(r) - 1 \approx -0.1$  according to the data in Fig. S5. However, our results show that even at large  $E$ ,  $I_{\text{cum}}(E)$  exhibits significant oscillation with no sign of convergence. The amplitude of oscillation is as large as the target value of  $g(r) - 1 \approx -0.1$ . This oscillation reflects the stripe-like feature in  $g(r, E)$  shown in Figs. 2 and S2, which represents the outgoing spherical waves of Compton scattered electrons. These stripes are part of the self-term of  $g(r, E)$ , and its integrated value is expected to asymptotically approach zero at infinite energy  $E$ , because  $g(r) = 0$  at  $r > 0$  for the self-term. Fig. S7 indicates that to achieve convergence  $g(r, E)$  has to be integrated up to very high energies. This observation seriously challenges the accuracy of the snapshot electron PDF determined by X-ray diffraction, because it suggests that the deviation of  $S_{\text{Diff}}(Q_{\text{EI}})$ , Eq. (1), from true  $S(Q)$  can be significant. On the other hand, the target value is achieved by integrating Eq. (S3) only up to 30 eV or so ( $\approx 2E_F$ ) where the contribution from the self-part is small. This again demonstrates the importance of energy range in evaluating electron correlation.

#### Supplementary Note 7. Decoupling of the dynamic structure factor within Random phase approximation

The double differential inelastic X-ray scattering cross-section for an electron gas is also defined by [S9]

$$\frac{d^2\sigma}{d\Omega dE} = \frac{r_0^2}{2\pi} \int \sum_{\mathbf{k}, \mathbf{k}'} \langle c_{\mathbf{k}}^\dagger(t) c_{\mathbf{k}+\mathbf{Q}}(t) c_{\mathbf{k}'+\mathbf{Q}}^\dagger(0) c_{\mathbf{k}'}(0) \rangle e^{-i(\frac{E}{\hbar})t} dt \quad (\text{S4})$$

where  $r_0$  is classical electron radius,  $c_{\mathbf{k}}^\dagger(t)$  creates a fermion with momentum  $\mathbf{k}$  at time  $t$ , and  $\langle \dots \rangle$  represents the quantum and thermal average. To compute the expectation value, decoupling is typically done through the random-phase approximation (RPA)

$$\langle c_{\mathbf{k}}^\dagger(t) c_{\mathbf{k}+\mathbf{Q}}(t) c_{\mathbf{k}'+\mathbf{Q}}^\dagger(0) c_{\mathbf{k}'}(0) \rangle \rightarrow \langle c_{\mathbf{k}+\mathbf{Q}}(t) c_{\mathbf{k}'+\mathbf{Q}}^\dagger(0) \rangle \langle c_{\mathbf{k}}^\dagger(t) c_{\mathbf{k}'}(0) \rangle \quad (\text{S5})$$

This decoupling erases the phase relationship between the initial and final states of the transition, thereby removing information about real-space correlation. For this reason,  $S(Q, E)$  has been viewed primarily via a single-particle excitation perspective, as described in the main text.

## References

- S1. W. Schülke, *Electron Dynamics by Inelastic X-Ray Scattering* (Oxford University Press, Oxford, 2007).
- S2. J. Als-Nielsen and D. McMorrow, *Elements of Modern X-ray Physics* (Wiley, 2011).
- S3. W. Schülke, H. Nagasawa, S. Mourikis, and A. Kaprolat, Dynamic structure of electrons in Be metal by inelastic x-ray scattering spectroscopy, *Phys. Rev. B* **40**, 12215 (1989).
- S4. N. W. Ashcroft and N. D. Mermin, *Solid State Physics*. (Saunders College Publishing, 1976).
- S5. J. P. Perdew and Y. Wang, Pair-distribution function and its coupling-constant average for the spin-polarized electron gas, *Phys. Rev. B* **46**, 12947 (1992).
- S6. D. Ceperley, Ground state of the fermion one-component plasma: A Monte Carlo study in two and three dimensions, *Phys. Rev. B* **18**, 3126 (1978).
- S7. D. M. Ceperley and B. J. Alder, Ground State of the Electron Gas by a Stochastic Method, *Phys. Rev. Lett.* **45**, 566 (1980).
- S8. W. Dmowski, S.O. Diallo, K. Lokshin, G. Ehlers, G. Ferre, J. Boronat, and T. Egami, Observation of dynamic atom-atom correlation in liquid helium in real space, *Nat Commun* **8**, 15294 (2017).
- S9. P. M Platzman and N. Tzoar, X-Ray Scattering from an Electron Gas. *Phys. Rev.* **139**, A410–A413 (1965).